Proceedings of the ASME 2024
International Mechanical Engineering Congress and Exposition
GT2024
June 24–28, 2024, London, England, UK

GT2024-128083

MULTISTAGE TURBOMACHINERY OPTIMIZATION FOR HIGH TEMPERATURE HEAT PUMPS WITH THE REVERSE RANKINE CYCLE

Robert Schaffrath[1,*], Panagiotis Stathopoulos[1], Andreas Schmitz[2], Eberhard Nicke[1]

[1]German Aerospace Center, Institute of Low-Carbon Industrial Processes
[2]German Aerospace Center, Institute of Propulsion Technology

ABSTRACT

The electrification of process heat generation will be a key to achieving carbon neutrality in the coming decades. One of the most promising approaches is to replace conventional heat supply systems with high-temperature heat pumps (HTHPs). A promising heat pump concept is based on the reverse Rankine cycle that uses water as its working fluid. By using turbomachinery for the compression process in this cycle, the performance of the HTHP can be increased compared to volumetric displacement systems, like screw or piston compressors. Although the design of the compressor geometry can be done sequentially in relation to the HTHP cycle design, better results can be obtained by an approach that integrates turbomachinery and the thermodynamic cycle design. Against this background, an automated optimisation method for a reverse Rankine HTHP with two radial turbocompressors in series is presented. In contrast to the current state of the art, the presented novel optimization approach uses 3D CFD data to calculate compressor performance. Furthermore, the integration of low fidelity compressor specific reduced order models are used to accelerate the gradient-free optimization process by a CO-Kriging surrogate model. The advantages of the novel approach are justified by comparing the numerical effort and the final values of the optimization objectives.

Keywords: Reverse Rankine Cycle, Turbomachinery optimization, Centrifugal Compressor

NOMENCLATURE

Roman letters

HTHP	High Temperature Heat Pump
CFD	Computational Fluid Dynamic
ECS	Environmental Control System
COP	Coefficient of Performance
CP	Compressor
ORC	Organic Rankine Cycles
DP	Design point
m	Meridional coordinate [−]
m'	Normalized meridional coordinate [−]
$RANS$	Reynolds-averaged Navier-stokes equation
SST	Saturated steam temperature
M	Mach number [−]
n	Relative rotational speed [%]
$\dot{m}$	Mass flow rate [$\frac{kg}{s}$]
x	Vapour quality [−]
h	Blade height [mm]
P_{th}	Thermal power output of HTHP [W]
COP	Coefficient of performance [−]
HFPC	High-fidelity process chain
LFPC	Low-fidelity process chain
HTOP	Highly throttled off-design point

Greek letters

α	Vector of free variables
α_{CP_1}	Vector of free variables of compressor stage 1
α_{CP_2}	Vector of free variables of compressor stage 2
β	Metal angle of blade [°]
β_{St}	Stagger angle of blade [°]
γ	Rake angle [°]
θ	Circumferential angle [°]
π^{loss}	relative pressure loss [−]
π_{ts}	Total-to-static pressure ratio [−]
η	Isentropic efficiency [−]
η_{ex}	Exergetic efficiency [−]

Superscripts and subscripts

1	Inlet stage 1
2	Outlet stage 1
3	Inlet stage 2
4	Outlet stage 2
t	Total condition
s	Static condition
1·	Impeller leading edge, location ·
2·	Impeller trailing edge, location ·
3·	Diffusor leading edge, location ·

*Corresponding author: robert.schaffrath@dlr.de

4· Diffusor trailing edge, location ·
·1 ·, location Hub
·2 ·, location Shroud

1. INTRODUCTION

The IPCC report states that limiting global warming to 1.5°C requires rapid and immediate reductions in greenhouse gas emissions [1]. In addition to the mobility and energy sectors, the industrial sector must adapt to reduce its emissions. In particular, heat generation for industrial processes needs to evolve from conventional coal, gas and oil-fired supply to emission-free solutions through electrification. High-temperature heat pumps (HTHPs) are a promising solution for the temperature range of 100 to 300 °C. The core unit of any heat pump is the compressor.

There are several types of compression systems that can be considered, such as volumetric displacement compressors ([2]), turbomachinery ([3, 4]) or two-phase water ejectors ([5]). The advantages of turbomachinery over displacement systems is the ability to increase overall performance by a very efficient compression process. Standalone water ejectors will not be suitable to achieve the required pressure ratios, but can act as a further step for compression. In addition, most heat pump applications will require more than one compressor stage to achieve the required temperature lift. As a result, the design of the turbo-compressor geometry must be tailored to the overall heat pump cycle and the required heat supply in terms of temperature and thermal power. Therefore, a design approach that considers the whole cycle, including the compressor performance, is preferred. In order to find the most suitable geometry for all compressor stages, an optimization approach should be regarded. Several publications can be found in the open literature that investigate the optimization of turbomachinery, including simulation of the thermodynamic system, which will be discussed in this section.

The integrated optimization approach, also known as zooming, has been successfully applied to the application of turbomachinery in aircraft engines. Follen et al. studied a one dimensional compressor model for performance calculation coupled with the zero dimensional thermodynamic cycle of a high pressure compressor [6]. Coupling of 2D flow data with thermodynamic cycle simulation was also part of investigation. A compressor-combuster test problem was published by Hendler et al. [7]. An adopted approach was presented by Schmeink and Schnös, comparing different coupling approaches [8]. In addition, 3D CFD information were also part of publications investigating coupled optimization problems. Pachidis et al. published a study with an aero engine test case [9]. An extended paper integrates a 2D throughflow method [10]. More recently, Pilet et al. investigated a zooming approach including 3D CFD and also mapping component models for a turbofan engine [11].

Integrated approaches have also been found in the literature for the design of turbomachinery used in Environmental Control Systems (ECS). Giuffre et al. published an integrated approach for a vapour compression cycle of an ECS, where the compressor performance was calculated by a reduced order model pre-trained on 165k synthetic data sets [12]. The same author presented another study for an integrated model considering a two-stage turbo for an ECS test rig [13].

Turbomachinery optimization for Organic Rankine Cycle (ORC) has also been considered for coupled design approaches. All found publications integrating 1D meanline methods to calculate the turbomachinery performance on different ORC setups and with different gas models [14–17] In the case of heat pumps, integrated turbomachinery optimization has also been studied. Giuffre et al. published an optimization for the design of the centrifugal turbo-compressor of a heat pump test rig [18]. The performance of the compressor system was calculated using a reduced order model based on scaling principles. One dimensional methods were also part of investigation for different kind of heat pump systems [19–25]. The methods have been applied to domestic heat pumps and HTHPs as well as to Rankine and Brayton based process architectures.

All aforementioned papers investigate coupled optimization approaches of turbomachinery and the overall thermodynamic cycle in different research areas. However, there is a lack of publications investigating integrated optimization using 3D CFD methods to calculate the performance of the turbomachinery. Only in the case of aero engine applications have studies been found that integrate 3D flow data, but these methods only consider axial machines. In particular, for energy conversion systems such as ORC or heat pumps, these methods cannot be directly applied because of the different types of turbomachinery used, the ways of coupling multiple stages, different working fluids and the overall thermodynamic cycle. Due to the fact that 3D blade design requires more free parameters an improved optimization strategy is necessary, in order to solve these optimization problems efficiently, by using data of multiple fidelities.

To the best of the authors' knowledge, this will be the first publication to fill this gap in the open literature by integrating 0D and 3D CFD flow data in a coupled optimisation between turbomachinery and thermodynamic cycle simulation for energy conversion systems. In addition, the application of the optimization problem is a two-stage HTHP based on the reverse Rankine cycle with water refrigerant providing heat at 180 °C., which is also an innovative energy conversion system.

The main advantage of using 3D CFD data instead of lower dimensional calculation methods is that it provides a more accurate prediction of the performance behaviour of the turbomachinery, resulting in a more accurate result for the overall thermodynamic cycle. In addition, the operating limits of turbomachinery are better predicted, resulting in a more efficient use of the system.

The paper is structured as follows, In the section 2, the optimization methodology is explained, including the parametrization, the CFD model and the cycle simulation in the case of a simple coupling model. The third section shows the results of the optimization and compares the simple coupling, without the integration of 0D data, with the multi-fidelity approach. The next section compares the baseline, based on the Casey-Robinson correlation, with the optimised geometries.

2. OPTIMIZATION METHODOLOGY

The gradient-free optimization algorithm is shown in Fig. 1. The optimization method is started by iterations where the vector of free variables α is randomly generated. This process is stopped after a fixed number of successful iterations. The next

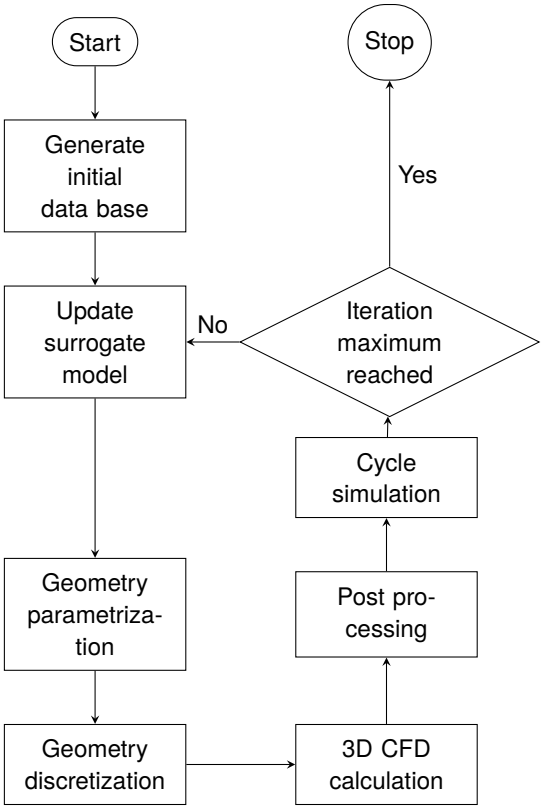

FIGURE 1: OVERVIEW OF OPTIMIZATION METHODOLOGY

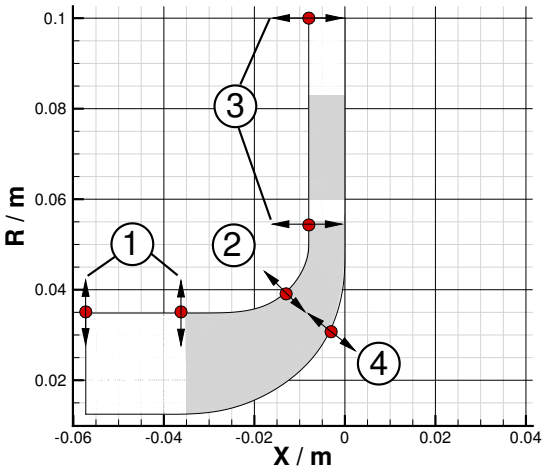

FIGURE 2: PARAMETRIZATION OF FLOW PATH OF COMPRESSOR STAGE 1

step is to update the ordinary Kriging surrogate model and use the expected improvement (more information on Kriging methods and infill criteria can be found in [26], [27] and [28]) for the infill criteria to define the values of α. The geometry of the two turbocompressors is then generated and discretized for the CFD calculation. The flow simulation is performed and turbomachinery performance parameters such as efficiency and pressure ratio are calculated. These parameters are used in the subsequent

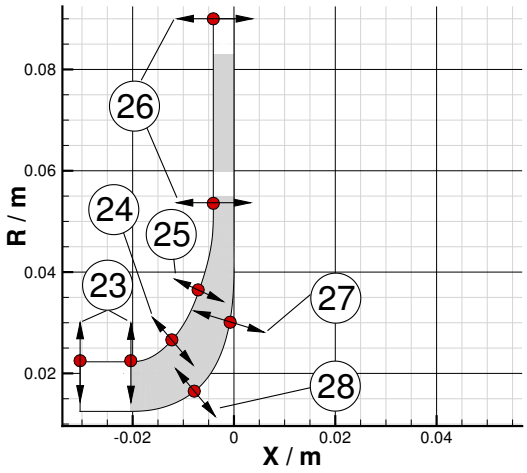

FIGURE 3: PARAMETRIZATION OF FLOW PATH OF COMPRESSOR STAGE 2

cycle simulation to calculate the HTHP objectives. If the maximum number of iterations are reached, the algorithm is stopped, otherwise the database is increased by the current iteration and the surrogate models are updated.

The whole optimization approach is implemented in AutoOpti, which was developed for the optimization of compressor geometries of aircraft engines ([29] and [30]), but could be successfully applied to the optimization of radial compressors for water vapour ([3] and [4]). The steps of parametrization, CFD model and cycle simulation are described in more detail in the following subsections. Sections 2.1, 2.2 and 2.3 present a coupling algorithm, called simple coupling because the optimization problem is solved in a straightforward manner. The following section presents an approach that uses the evaluation of different fidelities to improve the convergence of the optimization.

2.1 Parametrization

For the blade and vane design, the software BladeGen is used ([29]). The first step in designing the geometry is to discretize the flow path by adjusting the control points for the hub and the shroud line. Figure 2 shows the parametrization for compressor stage 1 and Fig. 3 for stage 2.In both figures, the grey area visualizes the blade and diffusor geometry in the meridional plane. For the first stage, the inlet radius, the degree of curvature across the chord at the hub and shroud and the height of the outlet can be modified by the optimizer. For the second stage, two additional control points for the curvature of the hub and shroud contour are added. The radius of the impeller outlet, the vane-less space between the rotor and stator and the length of the vanes are kept constant.

The next step is to define the β angle distribution for compressor stages 1 and 2, which is the angle between the meridional plane and the chord of the profile. Figure 4 shows the β angle for the initial geometry of the first stage including the degrees of freedom. The normalized meridional length m' was calculated by $dm' = \frac{\sqrt{dx^2+dr^2}}{r}$, with r radius of the impeller. The vaneless

TABLE 1: SUMMARY OF FREE PARAMETERS FOR OPTIMIZATION

	Name	Idx. Stage 1	Idx. Stage 2
Flow path	h_{12}	1	23
	Shift shroud 1	2	24
	Shift shroud 2		25
	h_{22}	3	26
	Shift hub 1	4	27
	Shift hub 2		28
β angle distribution	β_{11}	5	29
	m_{11}	6	30
	$\beta_{m_{21},1}$	7	31
	m_{21}	8	32
	m_{31}	9	33
	β_{21}	10	34
	m_{32}	11	35
	m_{22}	22	36
	$\beta_{m_{22},1}$	13	37
	m_{12}	14	38
	β_{12}	15	39
	β_{31}	16	40
	β_{41}	17	41
θ angle	$\beta_{St,11}$	18	42
	$\beta_{St,31}$	19	43
	$\beta_{St,12}$	20	44
	$\Delta\theta_{21}$	21	45
	CFD DP Backpressure	22	46

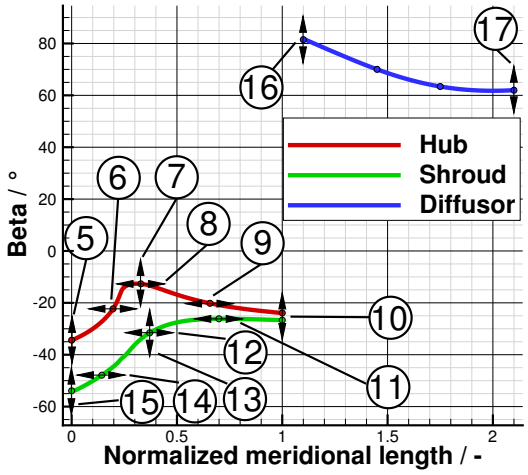

FIGURE 4: OVERVIEW OF β ANGLE DISTRIBUTION FOR COMPRESSOR STAGE 1

space between impeller and diffusor is 5 mm. It can be seen that two spanwise profiles are used for the impeller at the hub and shroud locations. Control points at the leading edge, three intermediate positions and the trailing edge define the shape of the impeller. The diffusor blades geometry is defined spanwise constant by using the same design parameters for the hub and

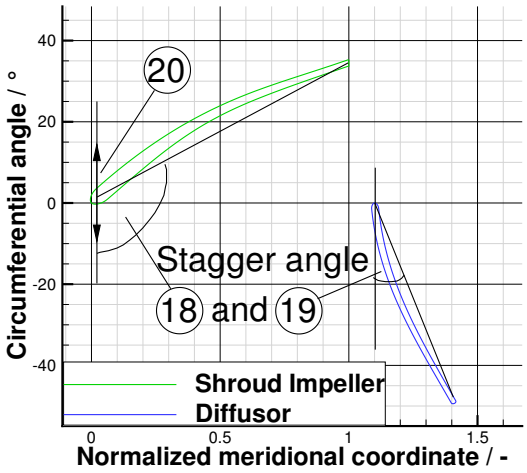

FIGURE 5: OVERVIEW OF STAGGER AND RAKE ANGLE DEFINITION FOR COMPRESSOR STAGE 2

shroud profile. It can be seen that only the β angle at the inlet and outlet defines the shape of the stator vane. The first stage has the same degrees of freedom for the β angle distribution as the second stage.

Based on the shape of the blades, the stagger β_{St} and the rake angle γ are defined in the meridional - circumferential (m-θ) coordinate system. The stagger is defined by the angle between the ordinate and the chord line connecting the leading and trailing edges. A circumferential shift of the impeller shroud profile defines the rake angle. The shroud profile of the impeller and the profile of the vane of the second stage can be seen in Fig. 5 for the baseline geometry. In addition, the hub profile of the impeller has an individual parameter for the stagger angle. Similar to the definition of the β angle, the first stage uses the same discretization approach.

In summary, the geometry of the first stage is discretized by 21 free parameters and the second stage by 23. The only difference is in the mentioned definition of the flow path. A summary of the free parameters for the optimization is shown in tab. 1.

2.2 Computational Fluid Dynamics

A 3D CFD method is used to calculate the flow through the two turbo compressors. In particular, a back-pressure controlled Reynolds-averaged Navier-Stokes (RANS) solver called TRACE is used ([31]). Only a segment of the rotating and stationary domain is considered with periodic boundary conditions. Furthermore, the impeller and stator are coupled by a mixing plane approach, where the mixing plane is located in the centre of the vane-less space. The MenterSST turbulence model is used for closing the RANS equations ([32]). The ideal gas model is used to calculate the thermodynamic properties and the Sutherland model is used to calculate the viscosity. The choice of using the ideal gas model was made to limit the numerical effort and because the considered operating range of the working medium is close to the thermodynamic field, where water steam can be treated as ideal gas, see [33, page 140]. The free stream tur-

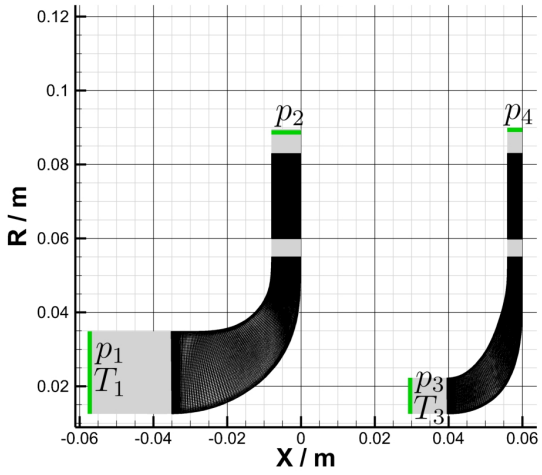

FIGURE 6: OVERVIEW OF INLET AND OUTLET DOMAINS OF BOTH COMPRESSOR STAGES

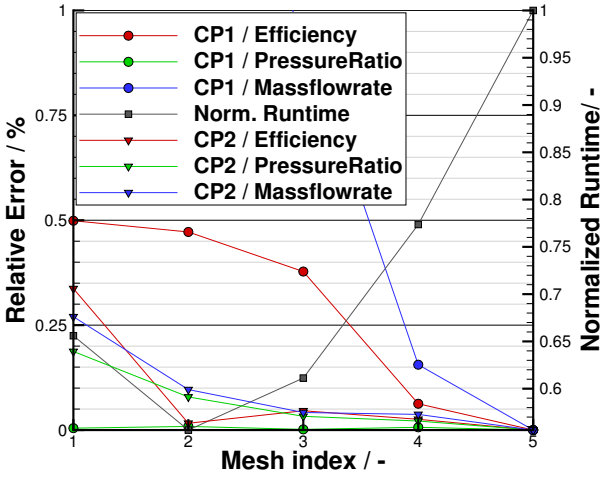

FIGURE 7: VISUALIZATION OF RELATIVE ERROR OF GRID INDEPENDENCE STUDY

TABLE 2: BOUNDARY CONDITIONS OF CFD MODELS

	Compressor 1	Compressor 2
Inlet	$p_t = 2$ **bar,** $T_t = 393.15$ **K**	$p_t =$ ㉒, $T_t \widehat{=}$ **SST**
Rotating wall	**adiabatic**	**adiabatic**
Viscous wall	**adiabatic**	**adiabatic**
Outlet	$p_t =$ ㉒	$p_t =$ ㊻

bulence intensity is set to 0.02 and a turbulence length scale of 0.0005 is considered. The value of the turbulent Prandtl number is regarded to be 0.9 and a second order scheme is used to discretise the advection terms in the Navier-Stokes equation.

The inlet and outlet regions of both stages are shown in Fig. 6. The inlet condition of stage 1 (p_{t1}, T_{t1}) is fixed, based on the HTHP cycle condition before the first compressor stage. In the outlet region, the static pressure (p_2) must be defined. To optimize the design point by the optimiser, the back pressure (p_2) is a free parameter for compressor stage 1. The inlet condition of the second stage (p_{t3}, T_{t3}) depends on the operating point of the upstream compressor stage and can be calculated as follows

$$\begin{aligned} p_{t3} &= p_2 * \pi^{loss}_{Cooler_1} \\ T_{t3} &= SST\,(p_{t3})\,. \end{aligned} \tag{1}$$

In the equation 1, $\pi^{loss}_{Cooler_1}$ is used for the relative pressure loss of cooler 1, which is located between compressor stages 1 and 2. The calculation of the saturated steam temperature for a given pressure is abbreviated as SST. The calculation is done using the open source package CoolProp [34]. The static pressure at the outlet of stage 2 is also a free parameter to modify the design point by the optimizer. Two assumptions have been made using this model description:

- Axial inflow conditions at both compressor stages and assuming, that no swirl is in the flow downstream cooler 1,
- neglecting the dynamic part of the pressure at the outlet of the compressor stage 1 and 2.

The first assumption is reasonable, since the remaining swirl downstream of a turbo compressor should be converted or disappear in a heat exchanger. Regarding the second assumption, in a preliminary study ([35, page 7]) for centrifugal steam compressors, it was found that for well designed vaned diffusers, low Mach numbers are determined at the outlet of the vanes, resulting in low losses in the volute. Consequently, the volute and the dynamic part of the pressure are not considered in this physical model, in order to decrease the computational time. Based on the previous CFD model description, for given geometries for both compressor stages and also static pressures p_2 and p_4, the calculations of both compressors can be separated and run in parallel in the optimization algorithm. An overview of all boundary conditions for both compressor stages is shown in Tab. 2. Free parameters are shown with ⊗ with index x

The discretization of both CFD models is done by the DLR internal meshing software PyMesh ([36]). The meshes consist of O-blocks around the blades, which resolve the near boundary layer, followed by C-blocks, which are open at the trailing edge, and H-blocks, which are used for the inlet, outlet and passage domains. The near boundary layers were refined until y^+ values below 1 could be determined. A mesh independence study was then performed. The initial mesh (468,000 volumes) was refined by a constant factor of 10% followed by calculation of the relative error for the turbo compressor parameters mass flow rate $\dot{m}$, total to static pressure ratio $\pi_{ts} = \frac{p_{2s}}{p_{1t}}$ and total to static isentropic efficiency $\eta = \frac{\pi_{ts}^{\frac{\gamma-1}{\gamma}} - 1}{\frac{T_{2t}}{T_{1t}} - 1}$ between the initial and refined meshes. Due to integer block sizes, the refined meshes result in slightly higher cell counts than 10% due to rounding. This process was repeated until all relative errors were below 0.25 %. The progress of the mesh independence study can be seen in Fig. 7. The mesh index on the abscissa corresponds to the mesh on

TABLE 3: OVERVIEW OF RELATIVE NUMERICAL ERROR OF GRID INDEPENDENCE STUDY

Mesh Idx.	Relative error in % of					
	η_{CP1}	π_{CP1}	$\dot{m}_{CP1}$	η_{CP2}	π_{CP2}	$\dot{m}_{CP2}$
1	0.499	0.005	2.657	0.337	0.187	0.270
2	0.472	0.009	1.411	0.016	0.079	0.096
3	0.378	0.002	0.957	0.046	0.033	0.042
4	0.063	0.007	0.156	0.026	0.021	0.037
5	0.000	0.000	0.000	0.000	0.000	0.000

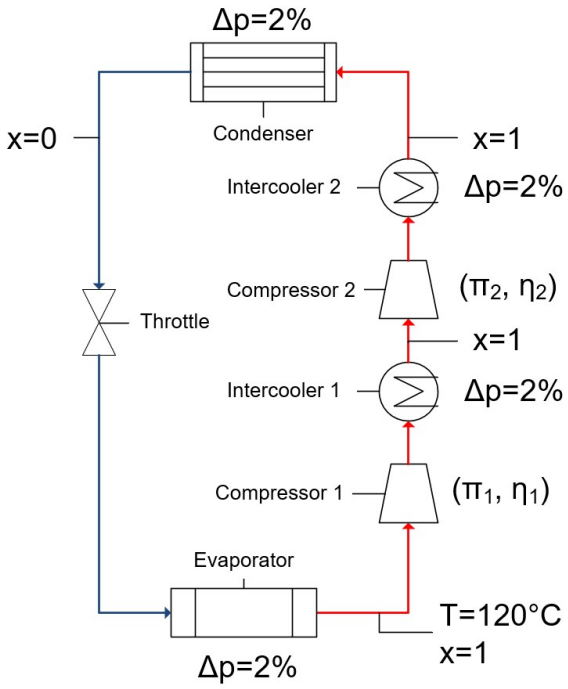

FIGURE 8: OVERVIEW OF THE INSTALLATION DIAGRAM OF THE HEAT PUMP

which the CFD has been calculated, with mesh index 1 being the coarsest mesh and mesh index 5 being the finest. In addition, tab. 3 shows the numeric values of the relative errors. The final mesh contains approximately 918,000 volumes. Furthermore, the normalised runtimes for the process steps parametrization, CFD discretization, CFD solution and post-processing are shown for both compressor stages. It can be seen that the normalized runtime increases dramatically with the refinement of the flow domain. The partitioning and distributed computation of the CFD solver was kept constant at 128 CPUs.

2.3 Cycle Simulation

The HTHP objectives are calculated by a subsequent thermodynamic cycle simulation. The thermodynamic cycle is not shown here, but can be seen in many books and publications, for example in [37] for a 3-stage HTHP. The Rankine HTHP consists of an evaporator, a condenser, two intercoolers, two turbomachines and a throttle. The refrigerant is water. The heat exchangers (evaporator, condenser and coolers) are modelled with a constant relative pressure drop of 2%, which is motivated on the one hand side by an averaged pressure loss, which is simulated with the test rigs of the DLR and can be also found in [25]. Only the primary side of the heat exchangers is considered, as it is assumed that sufficient waste heat is available in case of the evaporator and enough energy is absorbed by the secondary circuit at the condensor. The expansion valve reduces the pressure of the fluid without changing the enthalpy. The performance parameters of both turbomachines are defined at the design point based on the 3D CFD results. No off-design performance of the HTHP is considered. An overview of the installation diagram is shown in Fig. 8. The boundary conditions for the cycle simulation are also shown. In addition, on all connections, a mass flow rate of $\frac{\dot{m}_{CP1}+\dot{m}_{CP2}}{2}$ is defined, which ensures mass conservation in all components. Before the first compressor stage, saturated steam with a pressure of 1.99 bar is considered. The variable x is used for the vapour quality, with $x = \frac{m_{vapour}}{m_{total}}$. Based on this definition, $x = 1$ means the whole phase is saturated vapour and for $x = 0$ it is liquid water. For values in between, there is a mixture of both phases. The two intercoolers downstream of the compressors are designed to cool the gas to saturated steam temperature. In addition, there is no gas phase downstream of the condenser. The arrows connecting two components are shown in red when a pure gas phase is present and in blue otherwise.

For the two-stage HTHP, the thermal power output is calculated as the sum of the thermal powers of the condenser, cooler 1 and cooler 2:

$$P_{th} = P_{th}^{Condenser} + P_{th}^{1} + P_{th}^{2}. \tag{2}$$

In addition to that, the coefficient of performance of the HTHP is defined as the ratio of thermal power output to the sum of the electrical power consumption of both turbomachinerys:

$$COP = \frac{P_{th}}{P_{el}^{Compressor_1} + P_{el}^{Compressor_2}} \tag{3}$$

For the calculation, the open source python package Tespy is used. Tespy implements an iterative Newton-Raphson algorithm that solves a linear system of equations for the primary variables of mass flow rate, pressure, enthalpy and fluid mass fractions at all connections. More information about the cycle simulation solver can be found in [38].

2.4 Multifidelity Model

The coupling approach presented so far in this section does not take advantage of the fact that half of the free parameters in α modify stage 1 and the other half modify stage 2, and the results of both turbo compressors are coupled by a thermodynamic cycle simulation.

2.4.1 Low fidelity objective evaluation. In this subsection, an approach is presented that takes into account the structure of the optimization problem. In addition, the vector $\boldsymbol{\alpha}$ is split into $\boldsymbol{\alpha_{CP_1}}$ and $\boldsymbol{\alpha_{CP_2}}$, where α_{CP_1} contains all free parameters that control the performance of stage 1 (free parameter for the geometry and back pressure of stage 1) and α_{CP_2} of stage 2 (free parameter for the geometry and back pressure of stage 2 and back pressure of

stage 1), respectively:

$$\begin{aligned}\boldsymbol{\alpha} &= (\alpha_1, \ldots, \alpha_n) \\ &= \left(\alpha^1_{CP_1}, \ldots, \alpha^k_{CP_1}, \alpha^1_{CP_2}, \ldots, \alpha^l_{CP_2}\right) \\ &= \left(\boldsymbol{\alpha_{CP_1}}, \boldsymbol{\alpha_{CP_2}}\right)\end{aligned} \tag{4}$$

Based on this consideration of the vector α, the approach is to replace the 3D CFD calculation of the compressor performance of stages 1 and 2 by separate reduced order models (ROM), which will be called ROM_{CP1} and ROM_{CP2}. All of the ROM are implemented by Gaussian process regression models with constant mean, which is called ordinary Kriging (see [26]). In particular, three ROM_{CP1} are required to predict the efficiency, pressure ratio and mass flow rate of stage 1. These ROM depend only on the values of α_{CP_1} and not on the full vector of free variables α:

$$\begin{aligned}ROM^{\eta}_{CP1} &: \mathbb{R}^k \rightarrow \mathbb{R}^2, \boldsymbol{\alpha_{CP_1}} \rightarrow (\mathbb{E}(\eta), \mathrm{Var}(\eta)) \\ ROM^{\pi}_{CP1} &: \mathbb{R}^k \rightarrow \mathbb{R}^2, \boldsymbol{\alpha_{CP_1}} \rightarrow (\mathbb{E}(\pi), \mathrm{Var}(\pi)) \\ ROM^{\dot{m}}_{CP1} &: \mathbb{R}^k \rightarrow \mathbb{R}^2, \boldsymbol{\alpha_{CP_1}} \rightarrow (\mathbb{E}(\dot{m}), \mathrm{Var}(\dot{m})).\end{aligned} \tag{5}$$

For the prediction of the compressor parameters, only the mean of the Kriging model, which is denoted with $\mathbb{E}(\cdot)$, is used and not the uncertainty $\mathrm{Var}(\cdot)$. The ROM_{CP1} are preliminary trained to the optimization process on a dataset $\boldsymbol{\alpha_{CP_1}} \rightarrow (\eta, \pi, \dot{m})$ for variations of the compressor geometry 1. In addition, for the performance prediction of stage 2, three ROM_{CP2} are needed:

$$\begin{aligned}ROM^{\eta}_{CP2} &: \mathbb{R}^k \rightarrow \mathbb{R}^2, \boldsymbol{\alpha_{CP_2}} \rightarrow (\mathbb{E}(\eta), \mathrm{Var}(\eta)) \\ ROM^{\pi}_{CP2} &: \mathbb{R}^k \rightarrow \mathbb{R}^2, \boldsymbol{\alpha_{CP_2}} \rightarrow (\mathbb{E}(\pi), \mathrm{Var}(\pi)) \\ ROM^{\dot{m}}_{CP2} &: \mathbb{R}^k \rightarrow \mathbb{R}^2, \boldsymbol{\alpha_{CP_2}} \rightarrow (\mathbb{E}(\dot{m}), \mathrm{Var}(\dot{m})).\end{aligned} \tag{6}$$

Similar to stage 1, a dataset $\boldsymbol{\alpha_{CP_2}} \rightarrow (\eta, \pi, \dot{m})$ for compressor stage 2 is used. The motivation for this method is that the prediction of the stage-specific ROM is more accurate compared to a model trained on the full vector α, because the dimension of α_{CP_i} is about half the dimension of α. Furthermore, the numerical effort of the cycle simulation is negligible compared to the 3D CFD calculation, resulting in a very efficient way to calculate the HTHP objectives, by only evaluation the stochastic ROM and the thermodynamic cycle simulation.

2.4.2 Comparison to simple coupling. This results in two ways of calculating the objectives of the optimization problem:

- A accurate and numerical complex method including 3D CFD calculation and thermodynamic cycle simulation (High-fidelity process chain (HFPC)) and
- a method based on ROM for the prediction of stage specific performance followed by the cycle simulation (Low-fidelity process chain (LFPC)).

Figure 9 shows the high and low fidelity process chain evaluation methods. For the calculation of the objectives within the optimization loop, including the fulfilment of the constraints, only the HFPC evaluations are suitable, because the LFPC results

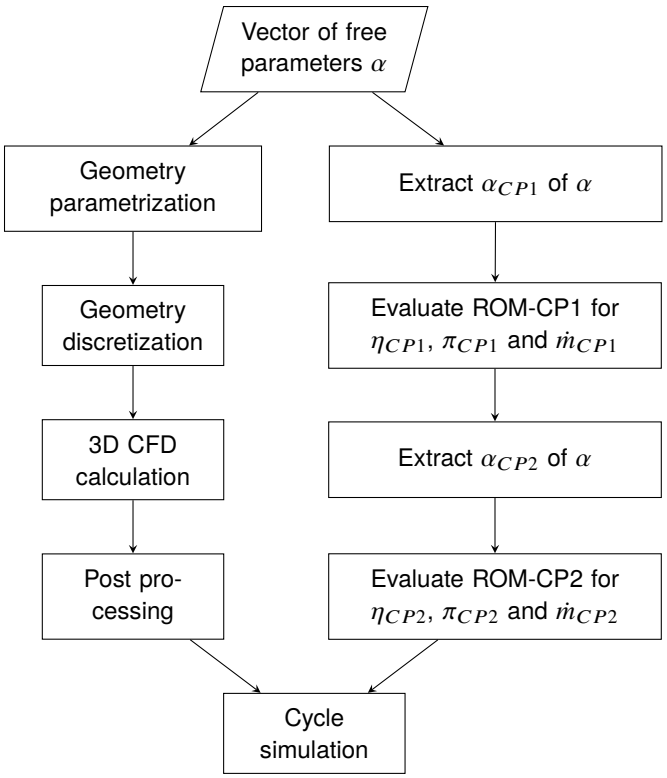

FIGURE 9: OVERVIEW OF HIGH (LEFT) AND LOW (RIGHT) FIDELITY OBJECTIVE EVALUATION

are biased due to poor predictions of the stage-specific performances. However, the LFPC evaluations can be used for a surrogate model that predicts the overall HTHP objectives based on the complete vector α and accelerates the optimization process. A co-Kriging method is used to combine data of different fidelities for the prediction. This type of surrogate model incorporates the LFPC evaluations by calculating the cross-covariance between the HFPC and LFPC. As a result of this approach, LFPC evaluation that are biased relative to HFPC have a negligible influence on the Co-Kriging prediction. More information on Co-Kriging and multi fidelity optimization can be found in [28].

3. OPTIMIZATION PROBLEM

One of the important parameters of a HTHP is the COP, which describes the ratio of thermal energy output to electrical energy input. Thermal power and temperature lift ΔT, which is defined as the difference between the temperatures at the heat sink and source, are also important parameters for the design of an HTHP. In addition, both turbo compressors should operate with the same mass flow rate. Another important characteristic is that the design point should not be close to the surge line of all compressor stages for safe operation. This is taken into account by a highly throttled off-design point (HTOP) with an increased back pressure of 2% compared to the design point for both turbomachines, which must converge. In this sense, 4 CFD simulations have to be calculated in each HFPC-iteration. Based on these considerations, the optimization problem can be

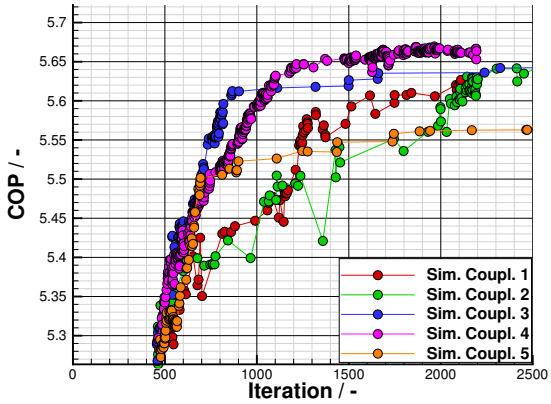

FIGURE 10: OVERVIEW OF CONVERGENCE HISTORY OF SIMPLE COUPLING APPROACH

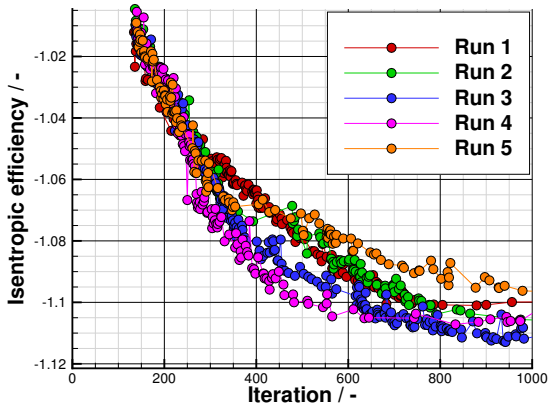

FIGURE 11: CONVERGENCE HISTORY OF TRUNCATED OPTIMIZATION FOR STAGE 1

formulated as follows:

$$\min_{\alpha} \quad -\frac{COP}{COP_{Baseline}} \tag{7a}$$

$$\text{subject to} \quad \frac{P_{th}}{1MW} \in [0.99, 1.01] \tag{7b}$$

$$\frac{\Delta T}{60K} \in [1.0, \text{inf}) \tag{7c}$$

$$\frac{\dot{m}_{CP1}}{\dot{m}_{CP2}} \in [0.99, 1.01] \tag{7d}$$

$$\text{HTOP converged} \tag{7e}$$

The vector α contains 21 geometry parameters for compressor stage 1 and 23 for stage 2. In addition, the back pressure used to define the design point for stages 1 and 2 increases the number of free parameters by 2. Therefore, the optimization presented here has to deal with a total of 46 free parameters, see Tab. 1.
The baseline geometries are derived by the Casey-Robinson correlation for given pressure ratios of 2.3 and mass flow rates of 0.4 $\frac{kg}{s}$ [39, Ch. 10]. The design point rotational speed is fixed at 100,000 rpm for both stages. By using the same speed for both compressors, they could be mounted on the same shaft to compensate for the axial thrust. None of the constraints were satisfied by the baseline geometries. The β angle distribution for the vaned diffuser is calculated from the impeller outflow β angle and the slip factor. To investigate the required blade thickness distribution for the impeller blades, a computational structural mechanics calculation was carried out for the baseline geometries, taking into account the rotational speed. The thickness distribution was manually iteratively modified at high stress locations until the material limits were reached. The material considered is a titanium alloy Ti-6Al-4V with a stress limit of 550 MPa. The blade thickness was then kept constant during the optimization procedure. The simple coupling optimization method is initialized by 200 randomly generated geometries based on the baseline.
Figure 10 shows the convergence history of the simple coupling approach. The optimization problem was started 5 times with the identical setup and stopped at a limit of 2500 iterations or when no objective increment could be stated. Only iterations that

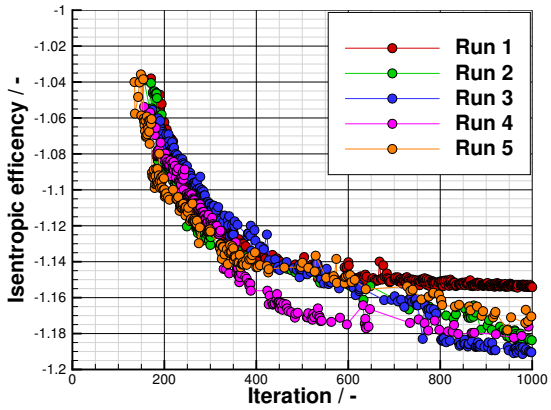

FIGURE 12: CONVERGENCE HISTORY OF TRUNCATED OPTIMIZATION FOR STAGE 2

satisfy all constraints are shown. All optimization runs require approximately 500 iterations until all constraints are satisfied and the objective is improved. Using the optimization method, the COP could be improved from 5.27 to 5.56 in the case of the worst optimisation run (5) and 5.66 in the case of the best run (4). This is a relative COP improvement of 5.5% and 7.4%, respectively.

To solve the optimization problem using the multi-fidelity approach, the first step is to create the databases for the stage individual ROM. This could be done by a Design of Experiment (DOE) that randomly distributes the samples of compressor geometries, but this would not take advantage of the fact that the most important parameter influencing the COP is compressor efficiency (see Eq. 3). Consequently, the databases for each compressor are generated by a truncated optimization with efficiency as objective. Both optimizations were stopped at 1000 iterations, which is a good compromise between accuracy and numerical effort for generating the databases. The convergence histories are shown in Fig. 11 and Fig. 12. Based on all successful iterations, ROMs for mass flow rate, pressure ratio and efficiency are trained

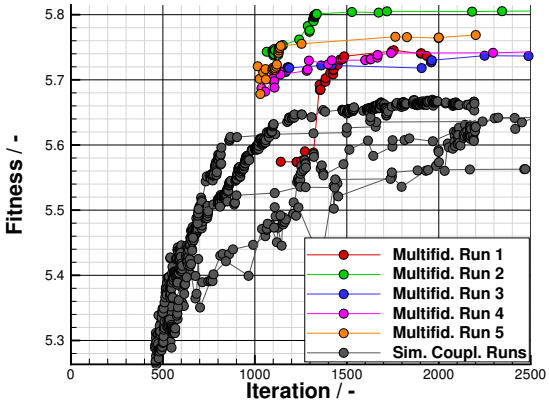

FIGURE 13: COMPARISON OF SIMPLE COUPLING (SEE FIG. 10) AND MULTI FIDELITY APPROACH

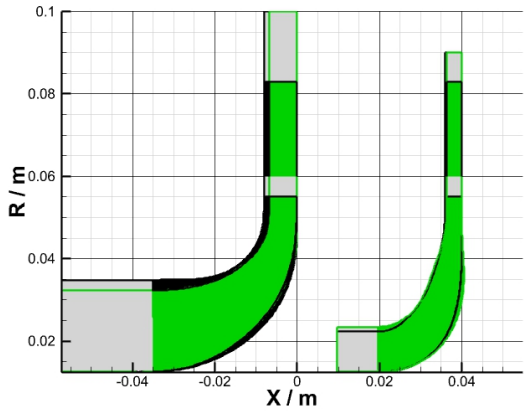

FIGURE 14: COMPARISON OF BASELINE (GRAY) AND OPTIMIZED (GREEN) FLOW PATH GEOMETRIES

for stage 1 and 2 respectively. A Gaussian process regression approximation [26] was performed for the ROM. Since the LFPC does not require a numerically complex 3D CFD calculation, the evaluation takes only about 30 seconds, which is extremely fast compared to the HFPC, which takes about 10 to 15 minutes. Due to the fast evaluation of the LFPC, only the HFPC evaluation is taken into account when calculating the total numerical effort. The decision whether the next evaluation is an HFPC or an LFPC is randomised with a probability of 90% for an LFPC and 10% for an HFPC. The multi-fidelity optimization is initialized with 1000 iterations, resulting in approximately 100 HFPC and 900 LFPC evaluations.

Figure 13 shows the comparison of the simple coupling with the multi-fidelity approach. The iteration counter of the multi-fidelity plots is shifted by 1000 iterations, which corresponds to the numerical effort of generating the database of the two stage-specific ROMS, since 4 CFD calculations are required for an HFPC evaluation and 2 x 2 CFD calculations for a stage-specific evaluation including the off-design convergence constraint.

Comparing the simple coupling runs (shown in grey) with the multi-fidelity runs, it can be seen that all multi-fidelity runs lead to higher objective values and also show converging behaviour from 1500 iterations. The best multi fidelity run (2) results in a COP slightly above 5.8, which is a relative improvement of 10%. The improvement can also be expressed in terms of the exergetic efficiency η_{ex}, which is defined as the ratio of the realised COP to the Carnot COP, which is theoretically the best possible COP:

$$\eta_{ex} = \frac{COP}{COP_{th}} = \frac{COP}{\frac{T_{out}}{T_{out}-T_{in}}}. \tag{8}$$

The baseline geometries resulted in an exergetic efficiency of 0.69 that also does not fulfils the design constraints and the best optimized geometries in 0.77, which is a relative improvement of about 11.6%.

A nice detail can be seen by comparing the convergence history of multi-fidelity run 1 (Fig. 13, shown in red) with the final objectives of the optimizations for generating the databases for the stage-specific ROMs (Fig. 11 and Fig. 12, shown in red). The final objective for stage 1 is the mean of all the other runs, but for stage 2 the resulting value is lower than all the others. This results in a worse initial iteration for the multi-fidelity model, as can be seen in Fig. 13. Nevertheless, multi fidelity run 1 gives comparable values to runs 3 and 4, which had better initial conditions. In this sense, the multi-fidelity model is robust to variations in the underlying database for the stage-specific ROMs.

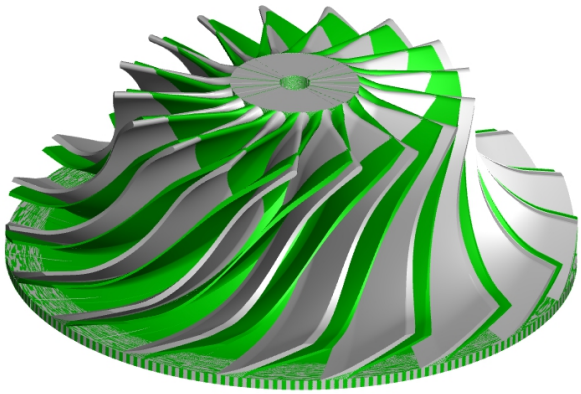

FIGURE 15: COMPARISON OF BASELINE (GRAY) AND OPTIMIZED (GREEN) IMPELLER GEOMETRIES FOR STAGE 1

4. RESULT INTERPRETATION

This section compares the baseline geometries and the resulting geometries of the best run (2) of the multi-fidelity method (COP=5.8, see. Fig. 13). The simple coupling approach was introduced to exploit the advantages of the multi fidelity approach hence the final geometry will not be compared to the baseline geometry. Figure 14 shows the flow path modifications obtained by applying the optimization approach. The baseline flow path is shown in gray and the optimized flow path is shown in green. The inlet blade heights of both stages are reduced by 13.9% and 18.3% as well as the outlet vanes by 11.3% and 11.1% to meet the required thermal power output of the HTHP and to ensure

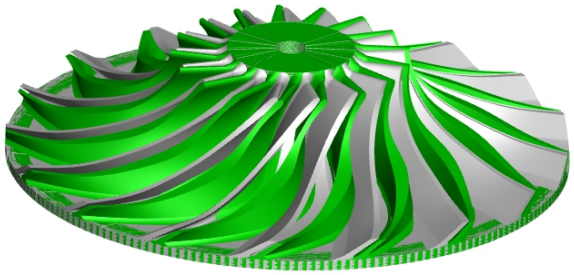

FIGURE 16: COMPARISON OF BASELINE (GRAY) AND OPTIMIZED (GREEN) IMPELLER GEOMETRIES FOR STAGE 2

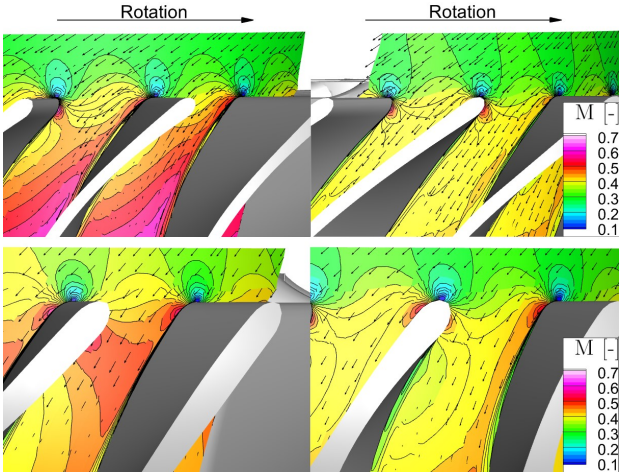

FIGURE 17: COMPARISON OF MACH NUMBER OF BASELINE (LEFT) AND OPTIMIZED (RIGHT) ROTOR BLADE FOR COMPRESSOR 1 (TOP) AND 2 (BOTTOM) AT 50% SPAWN

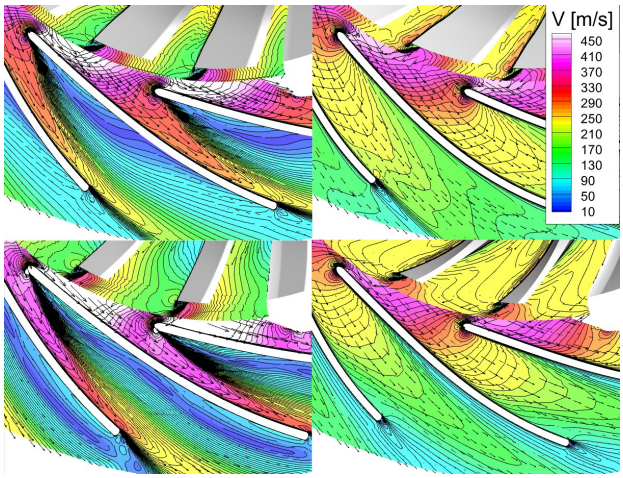

FIGURE 18: COMPARISON OF VELOCITY OF BASELINE (LEFT) AND OPTIMIZED (RIGHT) STATOR VANE FOR COMPRESSOR 1 (TOP) AND 2 (BOTTOM) AT 50% SPAWN

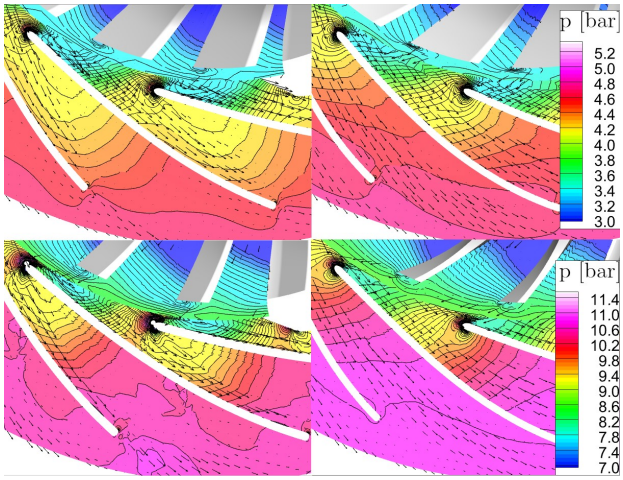

FIGURE 19: COMPARISON OF PRESSURE OF BASELINE (LEFT) AND OPTIMIZED (RIGHT) STATOR VANE FOR COMPRESSOR 1 (TOP) AND 2 (BOTTOM) AT 50% SPAWN

that both compressors operate at the same mass flow rate. The geometry comparison for the stage 1 impeller is shown in Figure 15 and for stage 2 in Figure 16.

The influence of the modified geometry on the flow at the inlet of the rotors can be seen in Fig. 17 at 50% spawn. The initial geometries are shown on the left and the optimized geometries on the right. The first line represents stage 1, the second stage 2. In the initial geometry of the first stage, it can be seen that the flow in the blade passage is strongly accelerated on the suction side and decelerated on the pressure side. The resulting secondary flow leads to losses in the inlet area. With the optimized geometry, the velocity difference between the pressure and suction side could be reduced by adjusting the beta angle. The angle was reduced by 9% at the hub and kept constant at the shroud, which corresponds to a reduction of 4.5% at mid spawn. As a result, the flow in the optimized geometry is almost incidence-free and a homogeneous velocity distribution at the inlet is achieved, which leads to reduced losses. Similar behaviour can be observed in the second compressor stage, but the reductions in the beta angles amount to a reduction of 12.6% and 6.2% at the hub and shroud, respectively.

The comparison of the absolute flow velocity between the initial geometry and the optimised geometry in the area of the stator is shown in Fig. 18. For the first compressor stage, it can be seen in the initial geometry that velocities greater than 450 m/s occur downstream of the impeller and absolute outflow angles α of only 19.4°. In the stator passage, this leads to an inhomogeneous velocity distribution and a flow separation bubble on the suction side. The flow pattern could be improved in the optimised geometry. The beta angle of the impeller was reduced by 8.6%, resulting in a 21.8% increase of the absolute outflow angle behind the impeller. This also reduced the speed below 400 m/s. The absolute outflow angle in combination with a 7.7% reduction of the beta angle of the stator leads to a more homogeneous speed distribution in the stator passage. The optimized beta angle increases the distance between the stator vanes by 40%, which leads to a reduction in the high velocities in the throat area. The

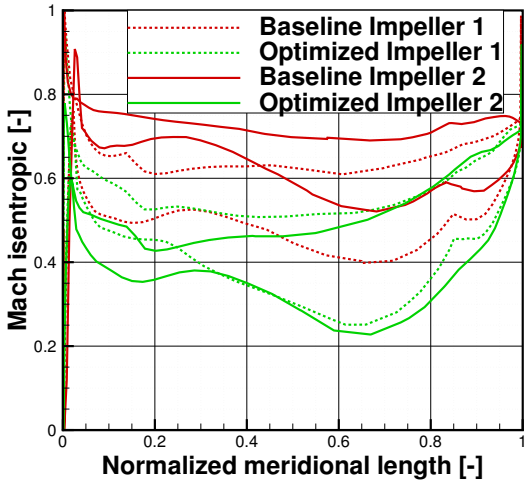

FIGURE 20: COMPARISON OF ISENTROPIC MACH NUMBER OF BASELINE AND OPTIMIZED IMPELLER FOR COMPRESSOR 1 AND 2 AT 50% SPAWN

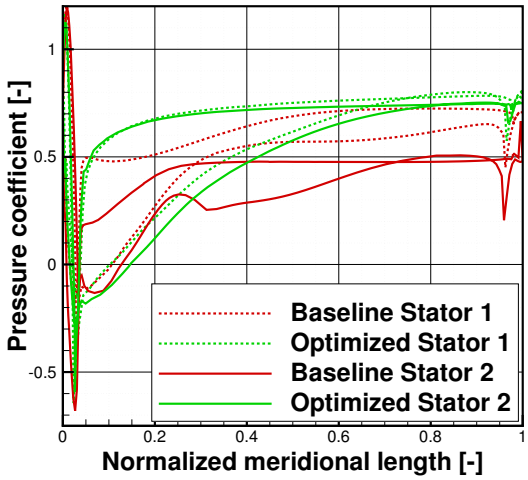

FIGURE 21: COMPARISON OF PRESSURE COEFFICIENT OF BASELINE AND OPTIMIZED STATOR FOR COMPRESSOR 1 AND 2 AT 50% SPAWN

flow separation in the diffuser was thus completely eliminated. A similar behaviour can be observed for the second stage, whereby the absolute outflow angle behind the impeller remains almost constant at 16°, but optimised beta angles of the impeller and stator contribute to reducing the separation of the flow. Fig. 19 compares the effects on the static pressure in the stator between the initial and optimised geometry. It can be seen that the optimised geometry allows a significantly greater proportion of the kinetic energy to be converted into static pressure by the stator. The numerical values of the baseline and optimized geometries for both stages can be seen in tab. 4.

The isentropic Mach number distributions for baseline and optimized geometry for the impeller is shown in Fig. 20 and the

TABLE 4: COMPARISON OF GEOMETRIC PARAMETERS OF BASELINE AND OPTIMIZED GEOMETRIES

	Stage 1		Stage 2	
	Baseline	**Optimized**	**Baseline**	**Optimized**
$h_{.1}$	22.30	19.73	9.76	10.90
$h_{.3}$	7.98	6.82	4.07	3.67
$\beta_{St,11}$	111.30	122.70	109.20	114.55
$\beta_{St,12}$	123.90	131.05	119.50	121.98
$\beta_{St,31}$	21.50	22.95	19.80	22.48
β_{11}	-34.40	-37.53	-31.30	-35.27
β_{12}	-57.50	-57.59	-43.50	-46.23
β_{21}	-27.70	-30.11	-25.20	-30.66
β_{31}	81.80	75.89	84.60	80.38
β_{41}	62.00	67.36	62.60	65.54

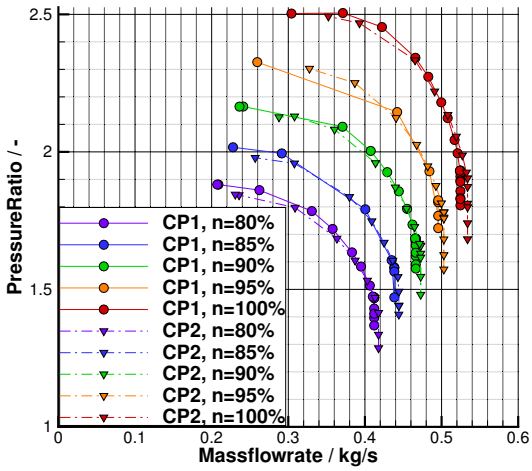

FIGURE 22: PRESSURE RATIO OF BOTH OPTIMIZED COMPRESSOR STAGES

pressure recovery coefficient for the stator geometries in Fig. 21. By using automated optimisation, the isentropic Mach number could be significantly reduced for both impellers. The pressure recovery for both stators was also increased to approx. 70%. The resulting performance maps are shown in Fig. 22 for the pressure ratio of both stages. The map of the second compressor stages is calculated by the outlet conditions of the first stage in the design point cooled down to SST level. Based on these stage specific maps, the resulting performance map is calculated by the exact map of stage 1 and a reduced map for the second stage depending on global flow coefficient ϕ_{t1} and tip speed mach number M_{u2}, in case of same rotational speeds for both stages, see [39, page 626]. Figure 23 shows the combined pressure ratio and Fig. 24 the isentropic efficiencies. The maps take into account the intercooler between stage 1 and 2, which cools the steam downstream of compressor 1 to SST level. The design point is indicated by a black square. In Fig. 18 it can be seen that the highly throttled off-design point considered results in a design point which has a descent distance to the surge line and ensures safe operation.

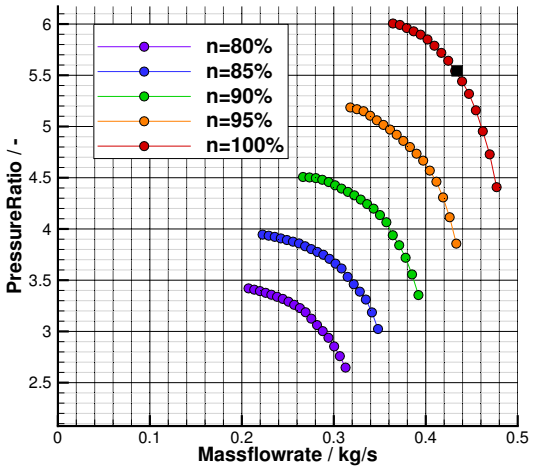

FIGURE 23: COMBINED PRESSURE RATIO OF BOTH OPTIMIZED COMPRESSOR GEOMETRIES INCLUDING THE INTERCOOLER BASED ON 2 BAR SST STEAM INLET CONDITIONS AND SAME ROTATIONAL SPEEDS

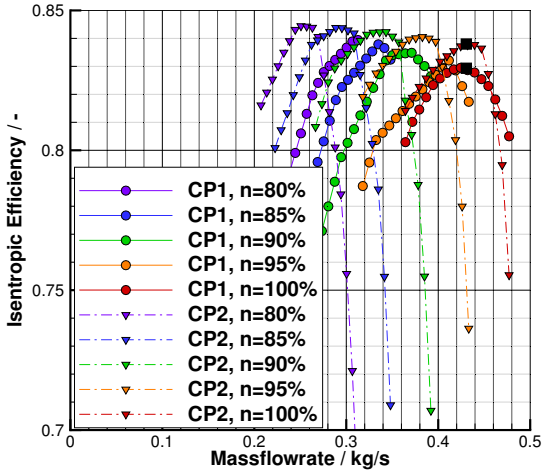

FIGURE 24: ISENTROPIC EFFICIENCIES OF BOTH OPTIMIZED COMPRESSOR GEOMETRIES INCLUDING THE INTERCOOLER BASED ON 2 BAR SST STEAM INLET CONDITIONS AND SAME ROTATIONAL SPEEDS

Overall, the performance map shows an acceptable range from choke to surge where the two-stage compression system can be used. In particular, the mass flow rate can be reduced by 14.3% in the direction of the surge line and increased by 10.7% in the direction of the choke line. This correlates in case of an decreased mass flow rate to an increased pressure ratio of 8.4% and decreased pressure ratio of 10% in case of and increase mass flow rate In Fig. 19, it can be seen that the design point is at the peak efficiency of both compressor stages.

5. CONCLUSION

The novel approach presented integrates 3D CFD data and 0D ROM data for evaluating the compressor performance, which is later used in the thermodynamic cycle simulation. The optimization process is accelerated by a CO-Kriging method, which uses compressor specific ROM, that are pre trained on truncated efficiency optimization per compressor stage. A comparison of the numerical effort and the COP improvement between the novel approach and a simple coupling using only 3D CFD data clearly shows the advantages of the method.

The application of the optimization is a novel 2-stage HTHP with water as refrigerant, providing heat at 180 °C. by using waste heat at a temperature of 120 °C. The objective of the optimization is the COP at the design point. Furthermore, a highly throttled off-design point is considered, as well as the thermal power of 1 MW and the temperature rise of 60 K by constraints.

The baseline geometries for turbo-compressors are derived by the Casey-Robinson correlation. The optimization resulted in the best case in a COP increment of 10% (5.8), while the baseline geometries delivered a COP of 5.27. In addition, the temperature lift of 60 K and the thermal power of 1 MW could be achieved. Comparing the exergetic efficiencies, the optimization could improve the baseline value from 0.69 to 0.77.

The optimization result shows a high potential to replace fossil fuel based energy systems with HTHP based on the Reverse Rankine Cycle. In particular, the high COP of 5.8 motivates further development of this research topic.

The next reasonable steps will be to integrate non-constant loss models for the heat exchangers, evaporator, cooler downstream of the compressors and condenser. In addition, the integration of a volute loss model, either data driven or analytical, could improve very well the accuracy of the model. Besides that, the integration of structural constraints for the impeller blades could further improve the optimization approach. Nevertheless, an improved gas model will be used in future studies. Finally, the inclusion of off-design performance in the optimization objective could improve the operating range and application of the HTHP.

REFERENCES

[1] IPCC. "Summary for Policymakers." *Summary for Policymakers. In: Climate Change 2023: Synthesis Report.Contribution of Working Groups I, II and III to the Sixth Assessment Report of the Intergovernmental Panel on Climate Change*. Geneva, Switzerland (2023).

[2] Utri, Matthias. "Entwicklung einer Hochtemperatur-Wärmepumpe mit Wasserdampf-Schraubenverdichter zur Wärme- und Prozessdampfbereitstellung." Version 1.0. Fraunhofer IEG (2024). Accessed February 19, 2024, URL https://www.ieg.fraunhofer.de/de/referenzprojekte/SteamScrew.html.

[3] Schaffrath, Robert, Kriese, Maximilian, Kajasa, Bojan, Köhler, Martino, Nicke, Eberhard and Voß, Christian. "Multi Operating Point Aerodynamic Optimization of a Radial Compressor Impeller for an Application in High Temperature Heat Pump." Vol. Volume 10D: Turbomachinery — Multidisciplinary Design Approaches, Optimization, and Uncertainty Quantification; Turbomachinery

General Interest; Unsteady Flows in Turbomachinery: p. V10DT34A011. 2022. DOI 10.1115/GT2022-82130. URL https://asmedigitalcollection.asme.org/GT/proceedings-pdf/GT2022/86120/V10DT34A011/6937206/v10dt34a011-gt2022-82130.pdf, URL https://doi.org/10.1115/GT2022-82130.

[4] Schaffrath, Robert, Nicke, Eberhard, Forsthofer, Nicolai, Kunc, Oliver and Voß, Christian. "Gradient-Free Aerodynamic Optimization With Structural Constraints and Surge Line Control for Radial Compressor Stage." Vol. Volume 13D: Turbomachinery — Multidisciplinary Design Approaches, Optimization, and Uncertainty Quantification; Radial Turbomachinery Aerodynamics; Unsteady Flows in Turbomachinery: p. V13DT34A005. 2023. DOI 10.1115/GT2023-101593. URL https://asmedigitalcollection.asme.org/GT/proceedings-pdf/GT2023/87110/V13DT34A005/7046131/v13dt34a005-gt2023-101593.pdf, URL https://doi.org/10.1115/GT2023-101593.

[5] Abu Khass, Omar, Tran, Anh Phong, Klöppel, Steffen and Stathopoulos, Panagiotis. "Modelling of Two-Phase Water Ejector in Rankine Cycle High Temperature Heat Pumps." Vol. Volume 5: Cycle Innovations: p. V005T06A003. 2023. DOI 10.1115/GT2023-101245. URL https://asmedigitalcollection.asme.org/GT/proceedings-pdf/GT2023/86984/V005T06A003/7044250/v005t06a003-gt2023-101245.pdf, URL https://doi.org/10.1115/GT2023-101245.

[6] Follen, Gregory and auBuchon, M. "Numerical Zooming Between a NPSS Engine System Simulation and a One-Dimensional High Compressor Analysis Code." (2000).

[7] Hendler, Marco, Lockan, Michael, Bestle, Dieter and Flassig, Peter. "Component-Specific Preliminary Engine Design Taking into Account Holistic Design Aspects." *International Journal of Turbomachinery, Propulsion and Power* Vol. 3 (2018): p. 12. DOI 10.3390/ijtpp3020012.

[8] Schmeink, Jens and Schnoes, Markus. "Automated Component Preliminary Design and Evaluation in the Overall Engine Using Fully Coupled Approaches." Vol. Volume 10D: Turbomachinery — Multidisciplinary Design Approaches, Optimization, and Uncertainty Quantification; Turbomachinery General Interest; Unsteady Flows in Turbomachinery: p. V10DT34A005. 2022. DOI 10.1115/GT2022-80634. URL https://asmedigitalcollection.asme.org/GT/proceedings-pdf/GT2022/86120/V10DT34A005/6937291/v10dt34a005-gt2022-80634.pdf, URL https://doi.org/10.1115/GT2022-80634.

[9] Pachidis, Vassilios, Pilidis, Pericles, Talhouarn, Fabien, Kalfas, Anestis and Templalexis, Ioannis. "A Fully Integrated Approach to Component Zooming Using Computational Fluid Dynamics." *Journal of Engineering for Gas Turbines and Power* Vol. 128 No. 3 (2004): pp. 579–584. DOI 10.1115/1.2135815. URL https://asmedigitalcollection.asme.org/gasturbinespower/article-pdf/128/3/579/5522170/579_1.pdf, URL https://doi.org/10.1115/1.2135815.

[10] Pachidis, Vassilios, Pilidis, P, Texeira, J and Templalexis, Ioannis. "A comparison of component zooming simulation strategies using streamline curvature." *Proceedings of The Institution of Mechanical Engineers Part G-journal of Aerospace Engineering - PROC INST MECH ENG G-J A E* Vol. 221 (2007): pp. 1–15. DOI 10.1243/09544100JAERO147.

[11] Pilet, Julien, Lecordix, Jean-Loi¨c, Garcia-Rosa, Nicolas, Bare'nes, Roger and Lavergne, Ge´rard. "Towards a Fully Coupled Component Zooming Approach in Engine Performance Simulation." Vol. Volume 1: Aircraft Engine; Ceramics; Coal, Biomass and Alternative Fuels; Wind Turbine Technology: pp. 287–299. 2011. DOI 10.1115/GT2011-46320. URL https://asmedigitalcollection.asme.org/GT/proceedings-pdf/GT2011/54617/287/2756371/287_1.pdf, URL https://doi.org/10.1115/GT2011-46320.

[12] Giuffre', Andrea, Ascione, Federica, Servi, Carlo De and Pini, Matteo. "Data-driven modeling of high-speed centrifugal compressors for aircraft Environmental Control Systems." *International Journal of Refrigeration* Vol. 151 (2023): pp. 354–369. DOI https://doi.org/10.1016/j.ijrefrig.2023.03.019. URL https://www.sciencedirect.com/science/article/pii/S0140700723000865.

[13] Giuffre', Andrea, Colonna, Piero and Pini, Matteo. "Design Optimization of a High-Speed Twin-Stage Compressor for Next-Gen Aircraft Environmental Control System." *Journal of Engineering for Gas Turbines and Power* Vol. 145 No. 3 (2022): p. 031017. DOI 10.1115/1.4056022. URL https://asmedigitalcollection.asme.org/gasturbinespower/article-pdf/145/3/031017/6958025/gtp_145_03_031017.pdf, URL https://doi.org/10.1115/1.4056022.

[14] Persky, Rodney, Sauret, Emilie and Ma, Lin. "Optimisation Methods For Coupled Thermodynamic and 1D Design of Radial Inflow Turbines." Vol. 1. 2014. DOI 10.1115/FEDSM2014-21665.

[15] Bahamonde, Sebastian, Pini, Matteo, De Servi, Carlo, Rubino, Antonio and Colonna, Piero. "Method for the Preliminary Fluid Dynamic Design of High-Temperature Mini-Organic Rankine Cycle Turbines." *Journal of Engineering for Gas Turbines and Power* Vol. 139 No. 8 (2017): p. 082606. DOI 10.1115/1.4035841. URL https://asmedigitalcollection.asme.org/gasturbinespower/article-pdf/139/8/082606/6177901/gtp_139_08_082606.pdf, URL https://doi.org/10.1115/1.4035841.

[16] Lampe, Matthias, De Servi, Carlo, Schilling, Johannes, Bardow, André and Colonna, Piero. "Toward the Integrated Design of Organic Rankine Cycle Power Plants: A Method for the Simultaneous Optimization of Working Fluid, Thermodynamic Cycle, and Turbine." *Journal of Engineering for Gas Turbines and Power* Vol. 141 No. 11 (2019): p. 111009. DOI 10.1115/1.4044380. URL https://asmedigitalcollection.asme.org/gasturbinespower/article-pdf/141/11/111009/6451881/gtp_141_11_111009.pdf, URL https://doi.org/10.1115/1.4044380.

[17] Schuster, Sebastian, Markides, Christos N. and White, Alexander J. "Design and off-design optimisation of an organic Rankine cycle (ORC) system with

an integrated radial turbine model." *Applied Thermal Engineering* Vol. 174 (2020): p. 115192. DOI https://doi.org/10.1016/j.applthermaleng.2020.115192. URL https://www.sciencedirect.com/science/article/pii/S1359431120305779.

[18] Giuffre, Andrea, Colonna, Piero and Pini, Matteo. "The Effect of Size and Working Fluid on the Multi-Objective Design of High-Speed Centrifugal Compressors." *International Journal of Refrigeration* Vol. 143 (2022): pp. 43–56. DOI https://doi.org/10.1016/j.ijrefrig.2022.06.023. URL https://www.sciencedirect.com/science/article/pii/S0140700722002092.

[19] Schiffmann, J. and Favrat, D. "Design, experimental investigation and multi-objective optimization of a small-scale radial compressor for heat pump applications." *Energy* Vol. 35 No. 1 (2010): pp. 436–450. DOI https://doi.org/10.1016/j.energy.2009.10.010. URL https://www.sciencedirect.com/science/article/pii/S0360544209004435.

[20] Schiffmann, J. "Integrated Design and Multi-objective Optimization of a Single Stage Heat-Pump Turbocompressor." *Journal of Turbomachinery* Vol. 137 No. 7 (2015): p. 071002. DOI 10.1115/1.4029123. URL https://asmedigitalcollection.asme.org/turbomachinery/article-pdf/137/7/071002/6301835/turbo_137_07_071002.pdf, URL https://doi.org/10.1115/1.4029123.

[21] Javed, Adeel, Arpagaus, Cordin, Bertsch, Stefan and Schiffmann, Jürg. "Small-scale turbocompressors for wide-range operation with large tip-clearances for a two-stage heat pump concept." *International Journal of Refrigeration* Vol. 69 (2016). DOI 10.1016/j.ijrefrig.2016.06.015.

[22] Meroni, Andrea, Zühlsdorf, Benjamin, Elmegaard, Brian and Haglind, Fredrik. "Design of centrifugal compressors for heat pump systems." *Applied Energy* Vol. 232 (2018): pp. 139–156. DOI https://doi.org/10.1016/j.apenergy.2018.09.210. URL https://www.sciencedirect.com/science/article/pii/S0306261918315290.

[23] Du, Yadong, Yang, Ce, Wang, Haimei and Hu, Chenxing. "One-Dimensional Optimisation Design and Off-Design Operation Strategy of Centrifugal Compressor for Supercritical Carbon Dioxide Brayton Cycle." (2021).

[24] Yao, Lichao and Zou, Zhengping. "A one-dimensional design methodology for supercritical carbon dioxide Brayton cycles: Integration of cycle conceptual design and components preliminary design." *Applied Energy* Vol. 276 (2020): p. 115354. DOI https://doi.org/10.1016/j.apenergy.2020.115354. URL https://www.sciencedirect.com/science/article/pii/S0306261920308667.

[25] Gollasch, Jens, Lockan, Michael, Stathopoulos, Panagiotis and Nicke, Eberhard. "Multi-Disciplinary Optimization Of Thermodynamic Cycles For Large-Scale Heat Pumps With Simultaneous Component Design." *Journal of Engineering for Gas Turbines and Power* (2023): pp. 1–35DOI 10.1115/1.4063637. URL https://asmedigitalcollection.asme.org/gasturbinespower/article-pdf/doi/10.1115/1.4063637/7048021/gtp-23-1354.pdf, URL https://doi.org/10.1115/1.4063637.

[26] Martins, Joaquim R. R. A. and Ning, Andrew. *Engineering Design Optimization*. Cambridge University Press, Cambridge, UK (2022). DOI 10.1017/9781108980647. URL https://mdobook.github.io.

[27] Aissa, Mohamed H. and Verstraete, Tom. "Metamodel-Assisted Multidisciplinary Design Optimization of a Radial Compressor." *International Journal of Turbomachinery, Propulsion and Power* Vol. 4 No. 4 (2019). DOI 10.3390/ijtpp4040035. URL https://www.mdpi.com/2504-186X/4/4/35.

[28] Schmitz, Andreas. "Multifidelity-Optimierungsverfahren für Turbomaschinen." Technical report no. Ruhr Universität Bochum. 2020. URL https://elib.dlr.de/140674/.

[29] Voß, Christian and Nicke, Eberhard. "Automatische Optimierung von Verdichterstufen." *Technische Informationsbibliothek Hannover* (2008).

[30] Voß, Christian, Aulich, Marcel and Raitor, Till. "Metamodel Assisted Aeromechanical Optimization of a Transonic Centrifugal Compressor." *1st TRACE User Conference*. 2014. URL https://elib.dlr.de/90969/.

[31] Franke, Martin, Kügeler, Edmund and Nürnberger, Dirk. "Das DLR-Verfahren TRACE: Moderne Simulationstechniken für Turbomaschinenströmungen." DGLR (ed.). *Deutscher Luft- und Raumfahrtkongress 2005*. 2005.

[32] Menter, Florian, Kuntz, M. and Langtry, RB. "Ten years of industrial experience with the SST turbulence model." *Heat and Mass Transfer* Vol. 4 (2003).

[33] Cengel, Y. A. and Boles, M. A. *Thermodynamics an Engineering Approach* (2005).

[34] Bell, Ian H., Wronski, Jorrit, Quoilin, Sylvain and Lemort, Vincent. "Pure and Pseudo-pure Fluid Thermophysical Property Evaluation and the Open-Source Thermophysical Property Library CoolProp." *Industrial & Engineering Chemistry Research* Vol. 53 No. 6 (2014): pp. 2498–2508. DOI 10.1021/ie4033999. URL http://pubs.acs.org/doi/pdf/10.1021/ie4033999, URL http://pubs.acs.org/doi/abs/10.1021/ie4033999.

[35] Kajasa, Bojan, Nicke, Eberhard and Kügeler, Edmund. "Numerical Investigation of a Thermally Perfect Gas Model for a Centrifugal Compressor Design With Water Vapor as Working Medium." Vol. Volume 13C: Turbomachinery — Deposition, Erosion, Fouling, and Icing; Design Methods and CFD Modeling for Turbomachinery; Ducts, Noise, and Component Interactions: p. V13CT32A009. 2023. DOI 10.1115/GT2023-101195. URL https://asmedigitalcollection.asme.org/GT/proceedings-pdf/GT2023/87103/V13CT32A009/7045748/v13ct32a009-gt2023-101195.pdf, URL https://doi.org/10.1115/GT2023-101195.

[36] Sauer, M. "An optimization based approach to multiblock structured grid generation." *6th European Conference on Computational Mechanics* (11-15 June 2018, Glasgow, UK).

[37] Kriese, Maximilian, Klöppel, Steffen, Setzepfand, Nico, Schaffrath, Robert and Nicke, Eberhard. "Part-Load

Behavior and Start Up Procedure of a Reverse Rankine High Temperature Heat Pump With Water As its Working Medium." Vol. Volume 5: Cycle Innovations: p. V005T06A027. 2023. DOI 10.1115/GT2023-103410. URL https://asmedigitalcollection.asme.org/GT/proceedings-pdf/GT2023/86984/V005T06A027/7044240/v005t06a027-gt2023-103410.pdf, URL https://doi.org/10.1115/GT2023-103410.

[38] Witte, Francesco and Tuschy, Ilja. "TESPy: Thermal Engineering Systems in Python." *Journal of Open Source Software* Vol. 5 No. 49 (2020): p. 2178. DOI 10.21105/joss.02178.

[39] Casey, Michael and Robinson, Chris. *Radial Flow Turbocompressors: Design, Analysis, and Applications*. Cambridge University Press (2021). DOI 10.1017/9781108241663.